



ELSEVIER

Contents lists available at ScienceDirect

Chemical Engineering Science

journal homepage: www.elsevier.com/locate/ces

Modelling soot deposition and monolith regeneration for optimal design of automotive DPFs



Janez Lupše^{a,1}, Marina Campolo^{a,*}, Alfredo Soldati^{a,b,c}

^a Dip. Politecnico, Università di Udine, Italy

^b Institute of Fluid Mechanics and Heat transfer, TU Wien, Austria

^c CISM, Udine, Italy

HIGHLIGHTS

- A 1D model is used to predict variation of DPF performances
- Filter loading capacity, back pressure and thermal response has been calculated
- Effect of cell density, filter permeability and thermal capacity has been assessed
- CSPI in the range [240–280] are the optimal choice for standard permeability filters.
- Optimal thermal management of filter can be achieved by simultaneously tuning of cell density, filter permeability and heat capacity.

ARTICLE INFO

Article history:

Received 8 February 2016

Received in revised form

27 April 2016

Accepted 3 May 2016

Available online 10 May 2016

Keywords:

Diesel particulate filter

Filtration

Soot deposition

Design optimization

Porous media

ABSTRACT

Diesel particulate filters (DPFs) are extruded monoliths comprising many square channels. The material of the monolith, and the size and shape of channels require optimization to guarantee best performances. In this work, we develop an original semi-analytical model to analyze filter behavior during both loading and regeneration operations. Fluid flow and pressure drop along/across monolith channels are calculated based on lubrication theory and Darcy sub-model. Time evolution of filter properties induced by soot deposition and cake formation is modelled using a unit collector sub-model. Cake burn-out and the thermal response of the monolith during the regeneration stage is modelled using a simplified soot combustion and heat transfer sub-model. The impact of channel number and size, filter hydraulic permeability and thermal capacity on back-pressure build-up, regeneration efficiency and risk of thermal failure are discussed to improve the design of automotive DPFs.

© 2016 Elsevier Ltd. All rights reserved.

1. Introduction

Diesel cars and heavy duty vehicles rely on after-treatment devices such as particulate filters to meet country-wide specific emission standards (e.g. EURO VI in Europe, Tier 4 in USA). DPFs are produced using monoliths of different materials, including porous ceramics (Cordierite), silicon carbide (SiC) or metal oxides (Aluminum Titanate, AT). Each monolith is made of many square channels (from 100 to 400 channels, or cells, per square inch, CPSI) (Adler, 2005), alternatively plugged at one end. Such configuration forces the engine's exhaust to flow through the porous wall of the channels, physically trapping particulate matter (PM) on the filtering surface. The material of the monolith, the size and shape of

the channels require optimization to guarantee best performances, i.e. high filtration efficiency and low pressure drop during standard operations, but also reliability and durability in the long run.

Channel design and filter material have not changed significantly over the years even if current generation filters are sometimes affected by problems, like incomplete regeneration and filter clogging due to repeated short trips in an urban start/stop environment, or occasional thermal failure of filter medium during regeneration. One of the main open issue is to guarantee both low back-pressure and high filtration efficiency during the normal DPF operating cycle. The material porosity and the pore size of a DPF should be as large as possible to ensure a low gas back-pressure. However, the size of the particles which can be efficiently filtered is strongly dependent on the pore size: the smaller the pore size, the larger the overall filtration efficiency. Recently, new, high efficiency filtering media with inhomogeneous wall structure (Bolterhoff et al., 2012) or optimized micro-structure (Nova et al., 2011)

* Corresponding author.

E-mail address: marina.campolo@uniud.it (M. Campolo).

¹ Now at: AVL-AST d.o.o., SI-2000 Maribor, Ulica kneza Koclja 22, Slovenia.

have been developed. These media could be used to produce ceramic monoliths with thinner porous wall whose reduced thermal inertia may speed up the regeneration process. However, a small thermal inertia may significantly increase filter temperature during soot oxidation, with larger risk of thermal failure.

Another open issue is the geometry of the monolith channels. Cross sections other than square (see Tsuneyoshi and Yamamoto, 2012; Patent US2013/0239532) are currently under development to increase the specific filtration surface (collecting area per unit volume of filter) and the soot loading capacity, thus decreasing the filter regeneration frequency.

The standard approach for filter design testing/optimization is to perform laboratory and numerical experiments: In both cases, improvement of filter performances is obtained through a trial and error procedure by running multiple tests. When the objective is to measure gross flow variables (e.g. back-pressure build-up during loading conditions, soot loading at regeneration, thermal resistance of filter medium) experiments and simulations can be done rather easily at a reasonable cost. When the objective is to derive more detailed information on the soot loading and regeneration dynamics to gain insights on the relevant physics involved, the complexity and cost of tests increase exponentially. Detailed experimental tests on DPFs are hard to perform because the monolith geometry is characterized by a large number of small and slender channels: It is very difficult to measure precisely spatially resolved quantities such as soot cake thickness or local temperature of filter wall as they evolve in time (see Bensaïd et al., 2009a, 2011; Martirosyan et al., 2010 to cite a few). Such space and time resolved measures are crucial to understand fully the physical and chemical processes controlling filter performance and to devise design alternatives for filter optimization.

In parallel with experiments, different types of numerical models have been used for filter testing/optimization. Sbrizzai et al. (2005) and Bensaïd et al. (2009b, 2010) used three dimensional Eulerian–Lagrangian and Eulerian–Eulerian models to investigate on the mechanisms controlling soot deposition inside the DPF and to predict the variation of filter performances over time. Deuschle et al. (2008) used a standard CFD code expanded with self-developed program routines to describe filtration, regeneration and deposit rearrangement effects in a DPF. Strom et al. (2011) examined the influence on particle deposition of small turbulence eddies penetrating the filter channels, and found that different deposition mechanisms may become important (Soldati and Marchioli, 2009). Because of the multi-scale geometry of the problem and the multi-phase nature of the flow, three dimensional simulations are too costly and time consuming to perform the preliminary screening of alternative DPF configurations. The customary approach is to rely on lumped parameters (i.e. zero dimensional) models such as those developed by Konstandopoulos et al. (2000), Konstandopoulos (2003) and Tandon et al. (2010). These models can be used to predict the evolution of gross flow variables but are inappropriate for design optimization.

A model best-suited for optimization purposes should account for the specific geometry of the filter, retain all the important physics involved in the soot deposition/regeneration process, and be efficient for repetitive use. Along these lines, efforts to devise such models have been made by Schejbal et al. (2009), Soldati et al. (2010) and Serrano et al. (2013) who developed one dimensional models to evaluate soot deposition. Bissett (1984), Piscaglia and Ferrari (2009) and Lee et al. (2009) developed one dimensional models to evaluate thermal regeneration. Recently, Bissett et al. (2012) and Kostoglou et al. (2012) proposed a correction to the standard one dimensional approach to account also for the spatial averaging adopted to simplify the calculations to one dimension.

To our knowledge, no attempt has been made up till now to use

one dimensional models for DPF design optimization. In this work we develop a model to predict the evolution of filter performances during both loading and regeneration operations. The model is based on the lubrication theory to characterize the flow along each channel of the monolith filter; flow through filter walls is evaluated by Darcy model and a unit collector sub-model is used to predict the dynamical change of material filter properties due to soot deposition. A simplified soot combustion and heat transfer sub-model is used to evaluate the local variation of filter wall temperature during the regeneration stage.

The model is validated with experimental data available from the literature and used to evaluate the impact of different design options (e.g. material properties such as porosity, pore size, hydraulic permeability, thermal capacity and conductivity; shape and size of filter channels) on back-pressure build-up, filter mass loading (or regeneration frequency) and thermal stresses produced during the regeneration stage.

The model is very time-efficient and allows the evaluation of a large number of alternatives before filtering device production, offering as a smart tool for the virtual screening of new design options.

2. Computational domain and modelling approach

2.1. Domain size and physical properties

The typical wall-through DPF used in passenger cars is a cylindrical block (diameter 0.15–0.30 m, length \approx 0.30 m) composed of a bundle of thin and long channels. Fig. 1 shows a sketch of the elementary unit of the filter, made of only two channels, with the relevant variables used to set up the model. In the reference coordinate system, x is the stream-wise direction, aligned with the channel main axis, and y is the wall-normal direction.

The flow that enters the monolith through channel 1 (dirty, the upper one in figure) is forced through the porous walls and exits through channel 2 (clean, the lower one in Figure). Soot particles entering with the flow (typical size about 100 nm, Tandon et al., 2010, and average density $\rho_{soot} = 1800 \text{ kg/m}^3$, Park et al., 2004) deposit in and along the porous wall. The clean filter channel size, $2H_2 = 2H_0$, remains constant in time (\approx 0.0015 m or lower) whereas the size of the dirty channel, $2H_1$, changes in time and space ($2H_1(x, t) = 2[H_0 - \delta_{cake}(x, t)]$) due to soot deposition (thickness δ_{cake}).

Typical working conditions during the loading stage correspond to isothermal flow of exhaust gas (average velocity 5–10 m/s upstream the filter, temperature \approx 550 K at the filter inlet). The flow of the gas approaching the DPF inlet is turbulent ($Re_{DPF} \approx 16,700\text{--}67,000$ based on filter diameter, approaching velocity, gas density and viscosity) and becomes laminar inside the channels a short transition length downstream the filter inlet section.

2.2. Balance equations

Fluid flow, pressure and temperature field inside the monolith can be described by three dimensional continuity, momentum and enthalpy balance equations. Since we are not interested in the 3D details of the flow and temperature field, each channel is considered axi-symmetric, switching to a 2D description of the problem. Two main directions (the stream-wise and wall-normal) exist inside the channel, and two different scalings can be used to describe the flow moving along and across the wall: the Reynolds number based on the channel length, L , and stream-wise velocity, U , $Re_L = \rho UL/\mu$, and the wall Reynolds number, based on the channel size, $2H_0$, and wall-through velocity, W , $Re_w = \rho W(2H_0)/\mu$.

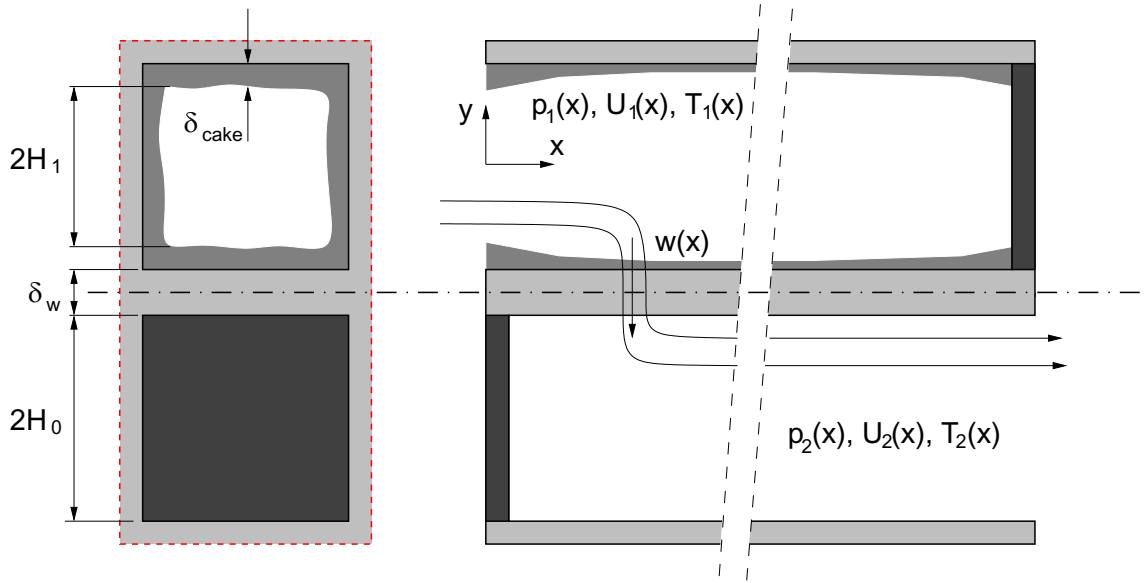


Fig. 1. Sketch of filter channels with relevant variables: pressure, p_i , temperature, T_i , average stream-wise velocity, U_i , and through wall velocity W . Subscript i identifies dirty (top, $i=1$) and clean (bottom, $i=2$) channels.

A third Reynolds number can be defined, $Re_H = \rho U (2H_0) / \mu$, based on stream-wise velocity and channel hydraulic diameter. These three Reynolds numbers are inter-related since $W \approx U (2H_0/L)$ from continuity equation and $Re_w \approx Re_L \cdot (2H_0/L)^2 = Re_H \cdot (2H_0/L)$, where $2H_0/L \ll 1$ is the channel aspect ratio that is very small for the specific geometry (slender channel, $2H_0/L \ll 1$). The Reynolds number Re_H reduces drastically at channel inlet compared to Re_{DPF} and due to the slender channel approximation also $Re_w \ll 1$. In these conditions, conservation equations simplify according to the lubrication theory and the model can be recasted into a 1D form in which the section averaged values of variables are solved for.

As discussed in Soldati et al. (2010) continuity and momentum equations can be written as:

$$\frac{d(2H_1)^2 \rho_1 U_1}{dx} = -P_w(x) \rho_w W(x) \quad (1)$$

$$(2H_0)^2 \frac{d\rho_2 U_2}{dx} = +P_w(x) \rho_w W(x)$$

$$U_1(x) = -\frac{4H_1^2}{\alpha\mu} \left(\frac{dp_1}{dx} \right); \quad U_2(x) = -\frac{4H_0^2}{\alpha\mu} \left(\frac{dp_2}{dx} \right) \quad (2)$$

where U_i and p_i are, respectively, average velocity and pressure in the dirty ($i=1$) and clean ($i=2$) channels, $P_w(x)$ and $W(x)$ are, respectively, the wetted perimeter of the channel and the filtration velocity at a reference filtration section (the clean channel surface), $\alpha = 28.26$ is the friction factor coefficient for square channel (Bissett, 1984; Bahrami et al., 2006) and ρ_i is the gas density at the local temperature of gas inside the dirty (1) and clean (2) channels and through the wall (w). Eqs. (1) and (2) can be combined into two second order differential equations describing the variation of pressure along the dirty and clean channels.

According to Darcy law, the filtering velocity at any given position x can be written as:

$$W(x) = \frac{K_{EQ}(x) [p_1(x) - p_2(x)]}{\mu [\delta_w + \delta_{cake}(x)]} \quad (3)$$

where μ is the fluid viscosity, $K_{EQ}(x)$ (m^2) is the equivalent Darcy

permeability, δ_w and $\delta_{cake}(x)$ are the wall and the local soot layer thicknesses, respectively. In a wall-through filter, the overall hydraulic resistance, $1/K_{EQ}$, is given by the sum of the local soot cake and the wall layer resistances:

$$\frac{\delta_w + \delta_{cake}}{K_{EQ}(x)} = \frac{H_0}{k_{cake}} \ln \frac{H_0}{H_0 - \delta_{cake}(x)} + \frac{\delta_w}{k_w(x)} \quad (4)$$

where k_w and k_{cake} are, respectively, wall and soot cake Darcy permeabilities (m^2). Overall hydraulic permeability may change significantly in space and time as the soot accumulates into and onto the filter wall, changing $k_w(x)$ and $\delta_{cake}(x)$. To simplify, in this work we will neglect changes in the cake permeability due to deposit restructuring and compaction during the loading phase, even if these changes occur inside a real DPF (see Liati and Eggenchwiler, 2010; Liati et al., 2012) and may have important consequences on soot reactivity. The unit collector model as described by Konstandopoulos et al. (2000) is used to calculate changes in wall filter porosity and permeability as the filter material gets progressively loaded (see Appendix A.1.2 for details).

When the size of soot particles is small ($D_p < 2 \mu m$), the multi-phase flow (gas plus soot particles) fed to the filter behaves as a pseudo-single phase see Bensaïd et al., 2009b): soot particles can be considered homogeneously distributed in the gas phase (with constant concentration $C = \dot{m}_{soot}/Q_{gas}$ in (kg/m^3) along the channel) and the soot mass flow rate filtering through the length dx of the channel can be written as:

$$\begin{aligned} d\dot{m}_{sep} &= 4 \cdot (2H_0) dx W(x) C = \Phi d\dot{m}_{sep} + (1 - \Phi) d\dot{m}_{sep} \\ &= d\dot{m}_{bed} + d\dot{m}_{cake} \end{aligned} \quad (5)$$

The two terms on the right represent soot accumulating into and onto the wall, i.e. deep bed and cake filtration (see Konstandopoulos et al., 2000 for details). The fraction $d\dot{m}_{bed}$ filtering through the wall is partially captured as it moves deeper and deeper. Collection efficiency is calculated from the joint effect of diffusion, interception and impaction mechanisms which depends on the local porosity, size of collectors and permeability. To account for the local variability of these quantities, the wall of the channel is modelled as a series of layers: the mass collected in each layer modifies the unit collector size and local properties of that layer and overall soot collection is obtained as a multistage

filtration efficiency (see Appendix A.1.2 for details).

The remaining part of filtering soot, $d\dot{m}_{cake}$, accumulates at the wall surface determining a continuous decrease of the inlet (dirty) channel size

$$H_1(t+1) = \sqrt{H_1(t)^2 - \frac{d\dot{m}_{cake}}{4\rho_{cake}dx}} \quad (6)$$

where ρ_{cake} is the soot cake density, and the corresponding increase of the soot layer thickness:

$$\delta_{cake}(t+1) = H_0 - H_1(t+1) \quad (7)$$

The final system of equations to be solved during the loading stage (i.e. for constant gas density) is:

$$\frac{d^2p_1}{dx^2} + \frac{4}{H_1(x)} \left(\frac{dp_1}{dx} \right) \frac{dH_1(x)}{dx} = \frac{\alpha H_0}{2H_1(x)^4} \frac{K_{EQ}(x)}{[\delta_w + \delta_{cake}(x)]} (p_1 - p_2) \quad (8)$$

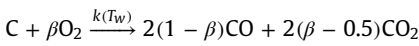
with boundary conditions $p_1(0) = p_{in}$ and $dp_1/dx(L) = 0$, and

$$\frac{d^2p_2}{dx^2} = \frac{\alpha}{2H_0^3} \frac{K_{EQ}(x)}{[\delta_w + \delta_{cake}(x)]} (p_1 - p_2) \quad (9)$$

with boundary conditions $dp_2/dx(0) = 0$ and $p_2(L) = p_{out}$. The system of Eqs. (8) and (9) has analytical solution for the clean filter with constant properties (see Soldati et al., 2010) whereas it should be solved numerically to account for the variation of channel size and wall properties observed during the loading stage.

2.3. Regeneration stage

Back-pressure build-up produced by soot accumulation inside the trap has to be periodically reduced through the regeneration of the filter, i.e. the oxidation of accumulated soot. The process is triggered by the increase of exhaust temperature at filter inlet, up to the soot oxidation temperature. In this work, thermal oxidation is modelled by the following chemical reaction (see Chen and Sun, 2013):



where β is an index for the completeness of thermal oxidation and $k(T_w)$ is the rate constant for thermal oxidation, given by a modified-Arrhenius equation (Bissett, 1985; Konstandopoulos et al., 2000; Chen and Sun, 2013)

$$k(T_w) = k_0 T_w \exp\left(-\frac{E_a}{RT_w}\right) \quad (10)$$

with $k_0 = 596 \text{ m}^2/\text{s K}$ and $E_a = 150 \cdot 10^3 \text{ J/mol}$ (Bissett, 1984). Oxygen in diesel exhaust is always enough to produce the complete oxidation of soot. The ratio of CO/CO₂ in the product gases depends on the supply of oxygen, and should be very low with excess of oxygen and temperatures lower than 800 °C (i.e. $\beta = 1$). However, Stanmore et al. (2001) report CO/CO₂ ratios mostly of order one even in these conditions, which would give $\beta = 0.75$. CO formation reduces the exothermicity of soot oxidation, limiting the heating rate of the support, whose temperature affects the progress of soot oxidation. Therefore, delayed regeneration and slower heating rate of the filter are expected when CO forms ($\beta < 1$).

In this work, we decided to use $\beta = 1$, i.e. to assume complete oxidation of soot to CO₂. This is a conservative assumption to test the thermal response of the filter because the heat released by soot oxidation, the heating rate of the support and the rate of reaction of soot will be maximum in this condition.

Assuming that transport along the channels is convection dominated, oxygen concentration is uniform in each channel, decreasing across the soot layer due to the thermal oxidation. The

balance for oxygen mass fraction Y in the wall-normal direction z inside the soot layer gives:

$$\frac{\partial}{\partial z}(WY) = -S_{react} Y k(T_w) \quad (11)$$

where S_{react} (m²/m³) is the specific surface of the soot layer. The amount of oxygen consumed per unit area, \dot{m}_{s,O_2} (kg/m² s) obtained integrating Eq. (11) across the soot layer δ_{cake} , is given by

$$\dot{m}_{s,O_2} = W\rho_w Y(0) \left\{ 1 - \exp\left[-\frac{S_{react} k(T_w) \delta_{cake}}{W}\right] \right\}$$

or by $\dot{m}_{s,O_2} = \dot{m}_{s,O_2}/MM_{O_2}$ in mole/m² s, with MM_{O_2} the molar mass of oxygen.

As indicated by the stoichiometric balance, $1/\beta$ moles of soot (i.e. carbon) will be oxidized for each mole of oxygen. Assuming that the cake density does not change in time during regeneration, the soot layer reduces according to following equation:

$$\frac{d\delta_{cake}}{dt} = -\frac{\dot{m}_{s,O_2} MM_c}{\beta \rho_{cake}} \quad (12)$$

with MM_c being the molar mass of soot. The heat released by the exothermic oxidation of soot depends on the number \dot{n} of CO₂ and CO moles formed (mole/s):

$$\dot{q}_{react} = \dot{n}_{CO} \Delta H_{CO} + \dot{n}_{CO_2} \Delta H_{CO_2} \quad (13)$$

and by their specific heats of formation (ΔH_i), and should be dissipated efficiently to avoid any critical increase of temperature inside the filter. Since the heat capacity of the solid phase (porous wall and soot layer) is much larger than that of the gas, a quasi-steady temperature variation is assumed for the gas. According to Bissett (1984), the conservation of energy for the gas moving along the two channels can be written as

$$\frac{d(2H_1)^2 \rho_1 c_{p,1} U_1 T_1}{dx} = -4(2H_0) [c_{p,w} \rho_w W T_w + h_1 (T_1 - T_w)] \quad (14)$$

$$(2H_0)^2 \frac{d\rho_2 c_{p,2} U_2 T_2}{dx} = 4(2H_0) [c_{p,w} \rho_w W T_w + h_2 (T_w - T_2)] \quad (15)$$

where $c_{p,i}$ is the gas heat capacity, T_i is the temperature, h_i is the convective heat transfer coefficient (see Bissett, 1984) and i identifies dirty (1), clean (2) and wall (w) conditions. For the solid phase, energy conservation is written as an unsteady heat balance:

$$\frac{d}{dt}(C_{all} T_w) = 4(2H_0) dx [h_1 (T_1 - T_w) - h_2 (T_w - T_2)] + \dot{q}_{react} - \dot{q}_{cond} \quad (16)$$

where $C_{all} = 4(2H_1) \delta_{cake} dx \rho_{cake} c_{cake} + 4(2H_0) \delta_w dx \rho_{wall} c_{wall}$ is the overall heat capacity of the solid wall and soot layer and \dot{q}_{cond} represents the conductive heat transferred along the solid filter given by

$$\dot{q}_{cond} = \lambda_{cake} \frac{d}{dx} \left[4\delta_{cake} (2H_1) \frac{dT_w}{dx} \right] + 4\lambda_w \delta_w (2H_0) \frac{d^2 T_w}{dx^2} \quad (17)$$

where λ_{cake} and λ_w are soot cake and wall conductivities, respectively, and $4(2H_1) \delta_{cake}$ and $4(2H_0) \delta_w$ are the areas across which conductive heat transfer occurs.

2.4. Numerical methods

The model solves mass, momentum and energy balance equations particularized for the loading and regeneration stage: transition from loading to regeneration can be triggered either (i) by the value of back-pressure at filter inlet, $p_1(0)$, exceeding a fixed threshold; or (ii) by the soot cake thickness exceeding a fixed fraction of the channel size; or (iii) by the soot loading exceeding a

specified value.

During loading, the time marching procedure is driven by the amount of soot depositing inside the filter: steady state conservation equations for isothermal flow ($\rho_1 = \rho_2 = \rho_w$), (Eqs. (8) and (9)) are solved at each time step changing the filter properties as the soot deposits into/onto the filter.

The solution algorithm proceeds in three steps: first, Eqs. (8) and (9) are solved using a trial value for the left boundary condition, $p_1(0)$, to obtain the gas pressure profiles along the dirty and clean channels. Equations are discretized in the stream-wise direction x using an implicit, second order finite difference method. The system is written in the compressed row storage (CRS) format (Saad and Wu, 1995) and solved by the conjugate gradients squared (CGS) solver with incomplete lower upper (ILU) preconditioning. Pressure profiles are then used to compute the flow along and across the wall using Eqs. (2) and (3). The trial boundary value $p_1(0)$ is iteratively updated to conserve the value of gas mass flow rate entering in the channel. Second, the soot mass flux along the inlet channel and through the wall is calculated using Eq. (5). Third, the deep bed filtration model is used to calculate the soot collected inside and on top of the porous wall and to determine the change in filter properties and soot cake thickness (Eq. (7)) for the next iteration.

Once triggered, the regeneration phase lasts for an user-defined time period (60 s in this work). During this stage, a step increase of gas temperature is imposed at the inlet boundary while keeping constant the mass flux of gas through the DPF. Balance equations for non-isothermal transport of mass, momentum and energy (Eqs. (14)–(16)) are solved for the gas and solid phases using a user-defined time step and neglecting the effect of soot deposition: since soot consumed by thermal oxidation determines a continuous change in cake thickness (Eq. (12)) and permeability, filter properties, pressure and flow distribution, and gas and filter temperatures along the channels are recalculated at each time step.

3. Results

3.1. Validation

To validate the model, we compared simulation results with experimental data of pressure drop measured during the loading stage of various Cordierite filter types (Murtagh et al., 1994) reported by Konstandopoulos et al. (2000). Filter channel geometry, material properties and test conditions used to perform the benchmark simulations are shown in Table 1 and correspond to Corning EX-47 and Corning EX-54 filter traps; data in brackets are values used by Konstandopoulos et al. (2000) to fit their OD filtration model, which are slightly different from values used as fitting parameters in our 1D model. Soot particle diameter considered for the simulations is 180 nm for EX-47 and EX-54 data.

The comparison between the pressure drop calculated by the model and the experimental data, shown in Fig. 2, indicates excellent agreement.

Fig. 3 shows additional information that can be extracted from the 1D model, which are not available from OD models. Fig. 3 (a) shows the evolution of section averaged velocity profiles calculated along the channel: results refer to EX-54 Cordierite filter. The stream-wise components of gas velocity along the dirty, U_1 (solid line with symbols) and clean, U_2 (solid line), channels (left axis) are shown together with the filtration velocity, W (dashed lines with symbols, right axis). Two stages of filtration are considered: The initial stage (open symbols), i.e. the clean filter, and later in time (closed symbols), when the filter is loaded by soot. At starting time, U_1 (open symbols) decreases and U_2 increases almost

Table 1

Test conditions used for model validation (taken from Konstandopoulos et al., 2000) corresponding to Cordierite filters EX-47 and EX-54. Values of model calibration parameters are the same used by Konstandopoulos et al. (2000); differences are shown in brackets.

Filter geometry		
Filter diameter, D_{DPF} (m)	0.2667 (10.5 in)	
Filter length, L (m)	0.3048 (12 in)	
CPSI (in^{-2})	100	
Wall thickness, δ_w ($\text{m}\cdot 10^{-3}$)	0.4318 (0.017 in)	
Number of cells (-)	8476	
Test conditions		
Flow rate (Nm^3/s)	0.236	
Gas temperature ($^{\circ}\text{C}$)	260	
Particulate mass (g/h)	18	
Filter medium		
Avg. pore size, $d_{p,0}$ (μm)	13.4	24.4
Porosity, ϵ_0	0.48	0.50
Clean filter permeability, $k_{w,0}$ ($\text{m}^2\cdot 10^{-13}$)	2.4	3.3
Soot characteristics		
Packing density (cake), ρ_{cake} (kg/m^3)	91.0	91.0
Cake permeability, k_{cake} ($\text{m}^2\cdot 10^{-14}$)	1.8	1.9
Packing density (wall), $\rho_{soot,wall}$ (kg/m^3)	7.10 (14.10)	6.24 (12.24)
Particle diameter (μm)	0.180	0.180
Percolation factor, ψ	0.9203	0.9246

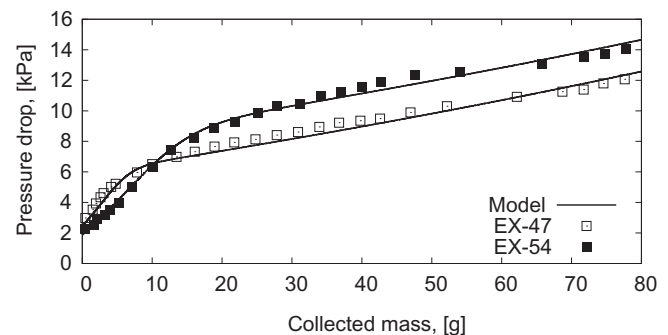


Fig. 2. Comparison between model results (line) and experimental data (symbols) by Murtagh et al. (1994) as reported in Konstandopoulos et al. (2000): data from EX-47 (open square) and EX-54 (closed square) filter tests.

linearly along the channel coordinate. These trends are unchanged at later stages of filtration and yet, as the soot builds up in the dirty channel (closed symbols) reducing its cross section, U_1 increases. Only minor variations in time are observed for U_2 . The filtration velocity profile (dashed line) changes significantly over time: In the initial stage of filtration (open symbols), W is larger at the inlet and outlet of the channel, promoting soot accumulation in these regions and changing the local permeability of the filter there. At later stages of filtration, due to the continuous build-up of the soot cake at the wall, W becomes more uniform along the channel.

Fig. 3(b) shows the evolution in time of δ_{cake} along the channel plotting δ_{cake}^* , the thickness normalized by the instantaneous channel length averaged value. Open and closed symbols identify the initial and final stages of filtration, respectively. The variability of cake thickness along the channel is maximum (from -4% to +8%) at starting time when the cake profile builds up following exactly the filtration velocity profile. Later on, due to the continuous change in filter properties produced by the accumulation of particles into and onto the wall, soot deposition becomes more uniform in space. These results are consistent with experimental and numerical data shown by Bensaid et al. (2009a, 2010) and they

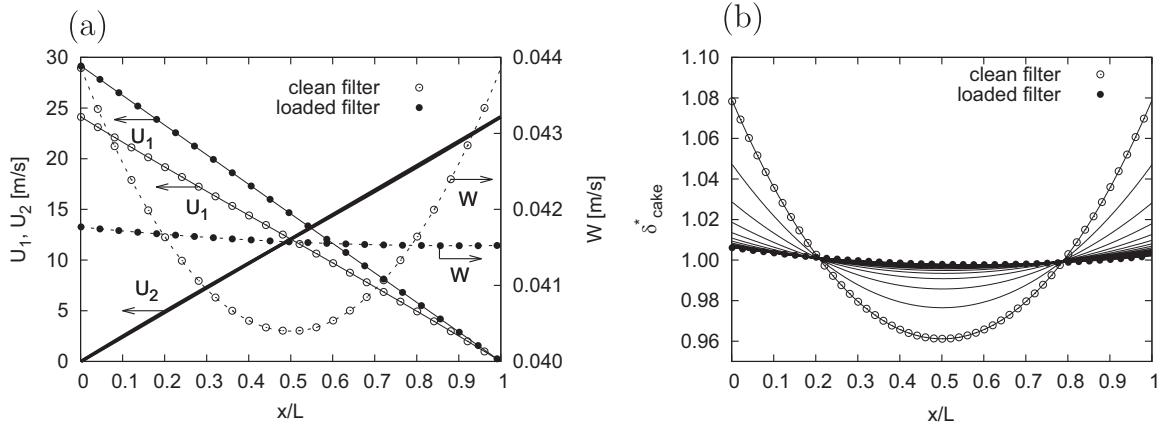


Fig. 3. Space and time variation of model variables: (a) stream-wise velocities, U_1 and U_2 (solid lines) and filtration velocity, W , profiles (dashed lines) along the channel; (b) dimensionless cake thickness. Open and closed symbols identify the initial stage and a later stage of filtration, respectively.

have been obtained at a fraction of the cost necessary to perform those experiments and complex 3D simulations.

3.2. Optimization

The validated model can be used to evaluate the effect of filter channel geometry and material properties on DPF performances during both loading and regeneration operations. Focusing on the loading stage, performances can be evaluated considering (i) the amount of soot accumulated inside the filter before the back-pressure rises too much for safe/efficient engine operations, or (ii) the maximum value of back-pressure reached at the end of the loading stage or (iii) the average value of back-pressure during the loading cycle; focusing on the regeneration stage, performances can be evaluated considering the thermal behavior of the monolith, evaluating (iv) the maximum temperature reached by filter wall during regeneration, or (v) the maximum temperature gradient, or considering (vi) how fast and complete is the regeneration process. A multi-objective optimization strategy should be used to identify the best filter configuration (i.e. filter material and geometry) since all these quantities are interrelated. In this work we focus on a subset of DPF characteristics only, starting from EX-54 Cordierite filter and exploring the impact of channel size variation when materials of different hydraulic permeability and different heat capacity are used (see Table 2).

Filter performances have been evaluated considering both a reference limiting value of back-pressure ($\Delta p = 16$ kPa) and a reference value of soot loading (7 g/L) as possible criteria triggering the filter regeneration. When the limiting back-pressure criterion is used, DPF performances during loading are evaluated using the average value of back-pressure calculated over the loading cycle and the amount of soot collected, which controls the duration of the loading cycle and the filter regeneration frequency; when the limiting mass criterion is used, performances are evaluated using the final and the average value of back-pressure calculated over

the loading cycle. For the regeneration stage, the maximum temperature reached by the filter wall during regeneration has been used as risk index of thermal failure for the filter support.

Simulations have been performed for a DPF filter with the same geometry of EX-54 (see Table 1) operating at the same conditions: the mass flux of gas and soot is kept constant for all the tests during both loading and regeneration operations; during regeneration, the temperature of exhaust gases at filter inlet is raised to 900 K for 60 s. This time period is sufficient to promote the complete regeneration of the filter whichever the soot load considered.

3.2.1. Effect of cell density

Variation of cell density (i.e. the number of CPSI) determines a change of the channel size which in turn affects (i) the specific collecting area, a_{coll} , i.e. the area available for soot deposition per unit volume of filter:

$$a_{coll} = 2\sqrt{CPSI} \left[1 - \delta_{wall}(t)\sqrt{CPSI} \right] \quad (18)$$

(ii) the blocking factor, defined as the ratio between the area open to the flow upstream and at filter inlet,

$$b_f = \frac{2}{\left[1 - \delta_{wall}(t)\sqrt{CPSI} \right]^2} \quad (19)$$

and (iii) the heat capacity of the filter wall

$$H_c \propto 2\sqrt{CPSI} \cdot \delta_{wall}(t) \left[1 - \delta_{wall}(t)\sqrt{CPSI} \right] (1 - \epsilon) \quad (20)$$

The variation of these three quantities as a function of CPSI and $\delta_{wall}(t)$ can be used to elucidate filter behavior during both loading and regeneration. Here, $\delta_{wall}(t) = \delta_w + \delta_{cake}(t)$ represents the wall thickness including the soot layer accumulated over time. Each of these parameters affects filter performance: δ_{cake} depends on a_{coll} , the pressure drop along the filter depends on b_f and δ_{cake} , and the rate of variation of filter temperature during regeneration is controlled by H_c .

Regeneration triggered by back-pressure threshold: Fig. 4 shows the change in filter performances versus cell density when the regeneration is triggered by a back-pressure threshold. Back-pressure build-up, Δp , versus collected mass per unit volume of filter, m_{filt} (which is equivalent to time under steady state loading conditions), up to $\Delta p = 16$ kPa is shown in Fig. 4(a). Different symbols identify different CPSI values. The arrow indicates the evolution of back-pressure build-up as the number of CPSI increases. The rate of back pressure build-up is steeper during the deep bed filtration stage and generally larger for those filter

Table 2

Hydraulic and thermal characteristics of filter supports of industrial use. Data are taken from Konstandopoulos (2003), Nemoto et al. (2011) and Boger et al. (2008).

Filter material	Cordierite	SiC	AT
Hydraulic permeability, $k_{w,0}$ (10^{-13} m ²)	3.3	28	28
Average pore size, $d_{p,0}$ (10^{-6} m)	24.4	40	40
Thermal conductivity, λ_w (W/m K)	0.8368	50	0.8368
Thermal specific capacity, c_{wall} (J/kg K)	1300	1900	2000
Thermal expansion coefficient (10^{-6} /K)	0.9	4	1
Max operating temperature (°C)	1300	1650	1000

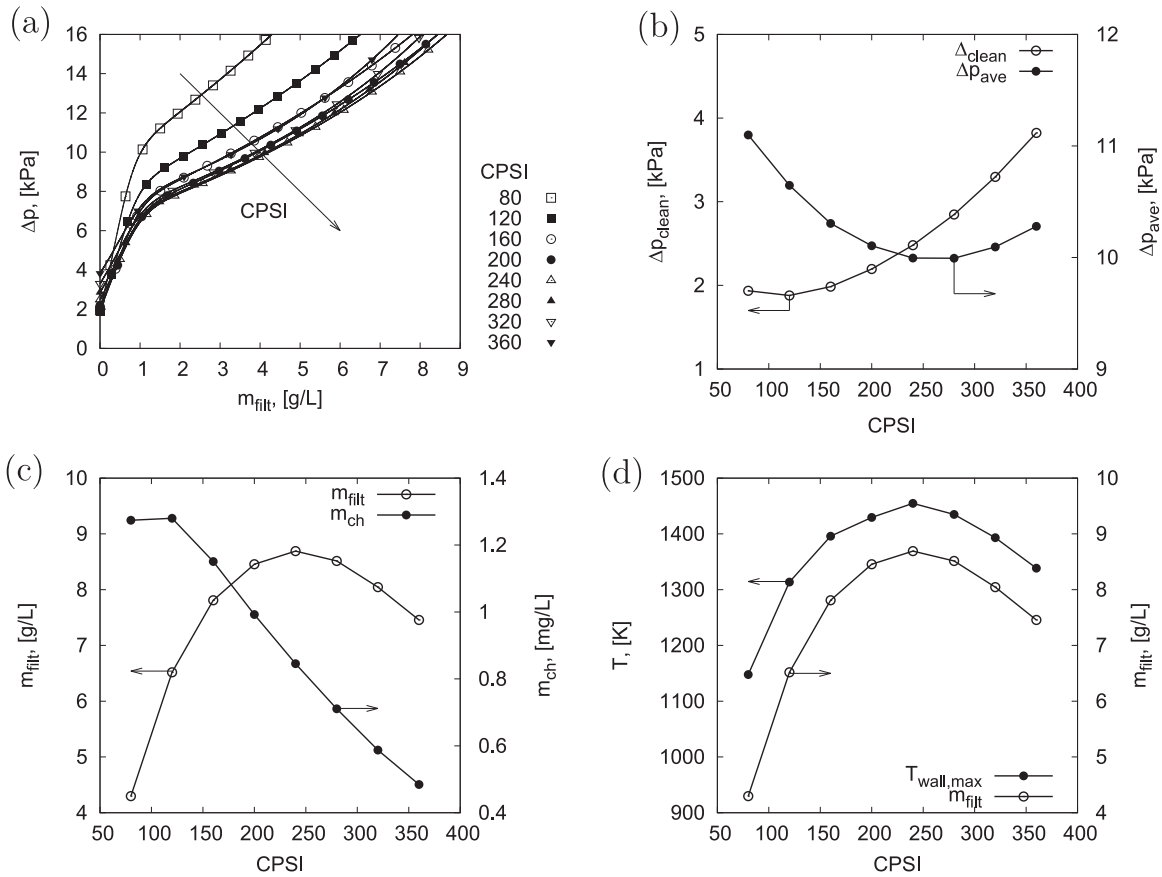


Fig. 4. Effect of cell density: (a) back-pressure, Δp , build-up over time during the loading stage; (b) variation of clean filter, Δp_{clean} , and time averaged back-pressure, Δp_{ave} ; (c) variation of mass collected inside the filter, m_{filt} , and per filter channel, m_{ch} ; (d) variation of maximum wall temperature during regeneration, $T_{wall,max}$, and mass collected per filter channel, m_{ch} . Regeneration triggered by back-pressure threshold ($\Delta p = 16$ kPa). (For interpretation of the references to color in this figure, the reader is referred to the web version of this paper.)

geometries characterized by small CPSI values. Back-pressure profiles become most similar for large CPSI values ($CPSI \geq 240$). For larger cell densities, the rate of back-pressure build-up during cake filtration is reduced due to the larger specific filtration area.

Fig. 4(b) shows the effect of filter geometry on clean filter pressure drop, Δp_{clean} (left axis), and back-pressure value averaged over the loading cycle, Δp_{ave} (right axis). Δp_{clean} has a minimum for $CPSI = 120$ and then increases with cell density, whereas Δp_{ave} decreases with CPSI and has a minimum for $CPSI \approx 240$ –280. Optimization of filter design based on Δp_{clean} or Δp_{ave} values would obviously lead to different conclusions.

Fig. 4(c) shows the values of soot loading for the whole filter, m_{filt} (left axis), and for one channel only, m_{ch} (right axis). m_{filt} increases reaching the maximum in the range $CPSI \approx 240$ –280, and then decreases again. Under steady state loading, the loading cycle can be longer (the filter loading capacity is larger) for filters with cell densities in that range. m_{ch} decreases with cell density, decreasing the amount of soot to be locally burnt during regeneration.

Fig. 4(d) shows the variation of peak temperature at filter wall, $T_{wall,max}$ (left axis), as a function of filter geometry. $T_{wall,max}$ varies in the range [1150–1450 K], which is less than the maximum operating temperature allowed for Cordierite filter (1573 K from Table 2). $T_{wall,max}$ appears to be well correlated with m_{filt} (right axis).

Fig. 5 shows the time history of filter wall temperature, T_{wall} (left column), and soot cake thickness, δ_{cake} (right column), calculated for CPSI 80, 240 and 360 (rows 1–3) to compare the progress in space and time of the soot regeneration process for these three different cell densities. In each picture, T_{wall} (or δ_{cake} , y-coordinate) is shown along the filter (x-coordinate) at different times

(lines with different colors, step 2 s). The gray-scale colorbox can be used to identify the specific time at which each temperature/soot thickness profile is drawn. The arrow indicates profile evolution over time. A large separation in space between gray lines indicates fast propagation of the thermal wave (or of the soot regeneration front) along the channel. The lower part of Fig. 5 (fourth row) shows the evolution of peak temperature, $T_{wall,max}$, and regeneration efficiency, η_{reg} , during regeneration time, t_{reg} . η_{reg} is defined as the ratio between the mass of soot already oxidized at time t and the soot loading when the regeneration starts. Symbols are used to identify the different cell densities.

Consider first results obtained for CPSI 80. Heating of filter wall (left column) is gradual in space and fast. Soot oxidation (right column) at each position along the filter needs about six seconds to complete, progressing at constant velocity from the upstream to the downstream section of the filter.

Soot thickness for CPSI 240 is larger than for CPSI 80 when the regeneration starts: the increase of filter wall temperature produced is larger and steeper in space. The thermal wave propagation speed is reduced. Wall heating is less uniform in space and time, with the largest value of temperature found at the end of the channel when the soot thickness goes back to zero (i.e. at the end of the regeneration).

The time history of temperature and soot cake thickness calculated for CPSI 360 is similar to CPSI 240. Nevertheless, the soot thickness along the channel is lower when the regeneration starts and the peak-value of temperature is reduced.

Comparing the evolution of peak temperature obtained for the three different cell densities we observe that the risk of thermal failure is the largest for CPSI 240: peak temperature rise during the

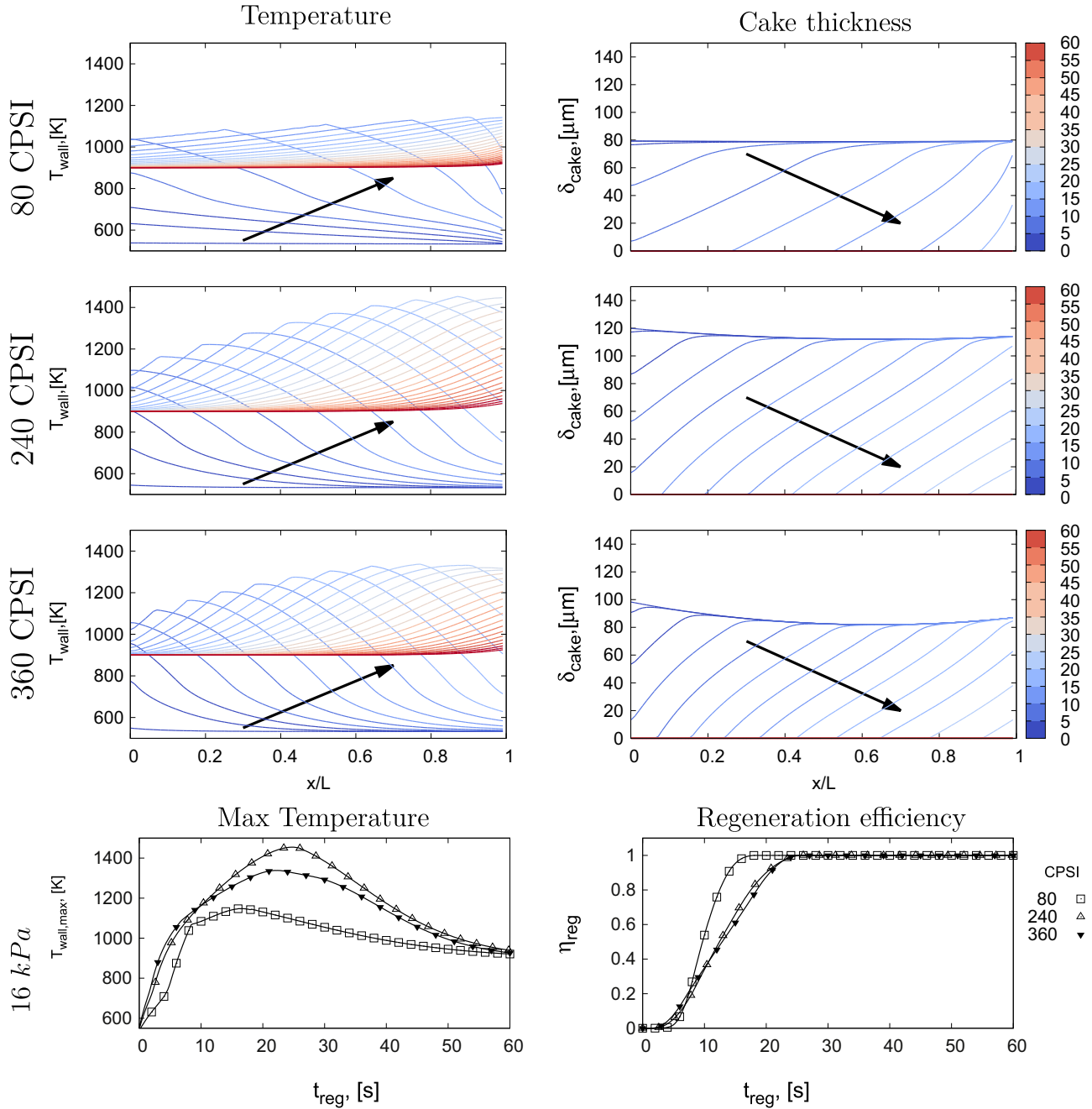


Fig. 5. Time history of filter wall temperature (left) and cake thickness (right) profiles during regeneration for CPSI 80, 240 and 360 filters (rows one to three). Time step is identified by line color (see right legend). Evolution of wall peak temperature, $T_{wall,max}$ (left) and regeneration efficiency, η_{reg} (right) during regeneration (fourth row). Regeneration triggered by back-pressure threshold ($\Delta p = 16$ kPa).

first seconds of regeneration is the largest, and peak temperature value is always larger than for any other cell density. The evolution of η_{reg} shows that regeneration is faster for CPSI 80. For this geometry, half of the soot load is burnt after 9.5 s, whereas the regeneration process takes 18.2 s to complete. For CPSI 240 (and 360), half of the soot load is burnt after 11.8 s (12 s), whereas the regeneration process takes 25.8 s (25.2 s) to complete.

Regeneration triggered by reference filter soot loading: Fig. 6 shows filter performances when the regeneration is triggered by the limiting value of soot load (or loading time under steady state loading conditions), $m_{filt,max} = 7$ g/L. Back-pressure build-up versus m_{filt} shown in Fig. 6(a) and in Fig. 4(a) is the same in the same range. Yet, Δp rises above 16 kPa for CPSI 80. Again, Δp changes slightly for $CPSI \geq 200$.

The effect of filter geometry on Δp_{ave} (right axis) and Δp_{clean} (left axis) is shown in Fig. 6(b). The clean filter pressure drop (the same as before) is shown for reference only. Also in this case, Δp_{ave} has a minimum at $CPSI \approx 240$ –280. This trend is similar to that shown in Fig. 4(b), indicating that optimization of filter geometry based on Δp_{ave} values seems to be independent from the selected regeneration mode.

Fig. 6(c) shows back-pressure values when the filter soot loading is 7 g/L, $\Delta p(7$ g/L) (left axis), and the mass collected along each channel, m_{ch} (right axis). $\Delta p(7$ g/l) is minimum in the range $CPSI \approx 240$ –280, indicating lower flow resistance for filters with larger cell density. m_{ch} decreases with CPSI value.

Fig. 6(d) shows the variation of peak temperature at filter wall, $T_{wall,max}$ (left axis), as a function of CPSI value. $T_{wall,max}$ varies in the

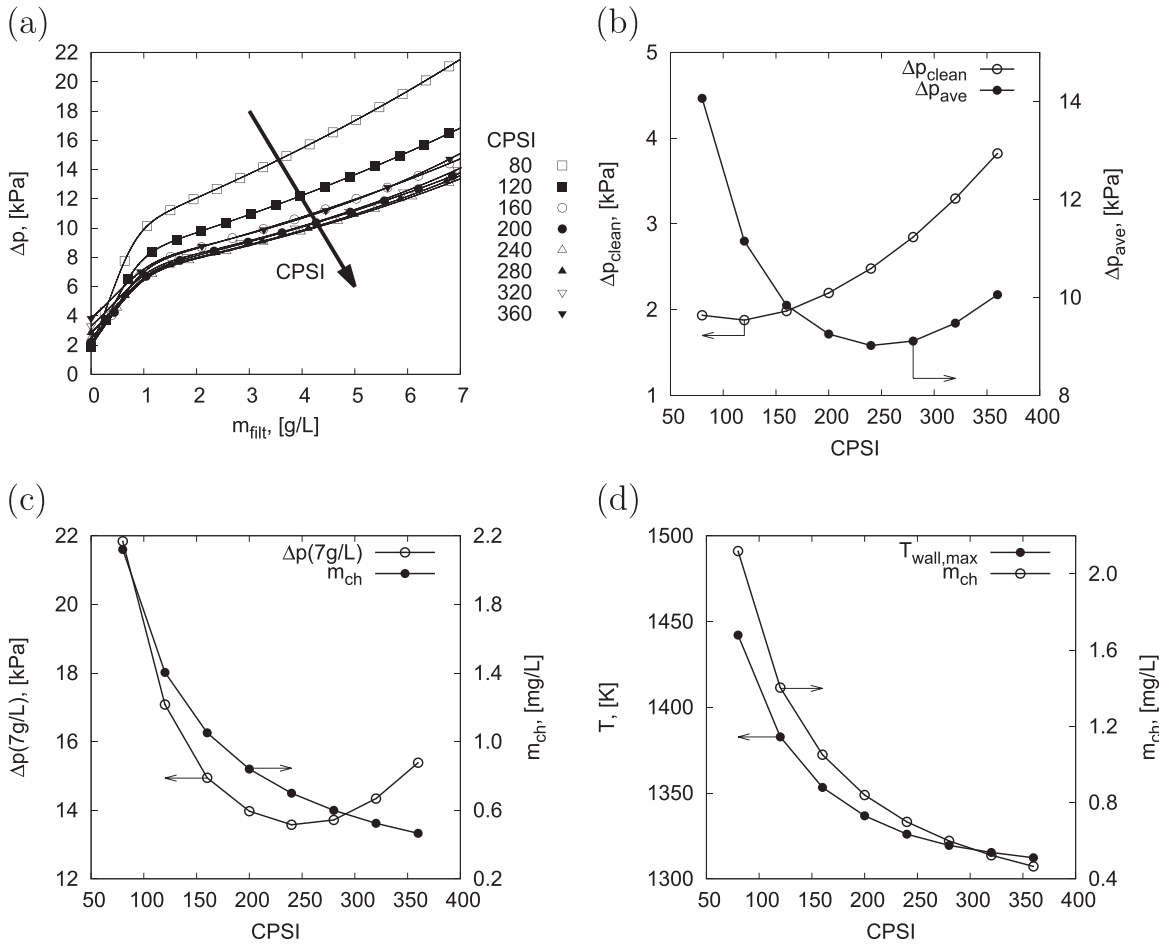


Fig. 6. Effect of cell density: (a) back-pressure, Δp , build-up over time during the loading stage; (b) variation of clean filter, Δp_{clean} , and time averaged back-pressure, Δp_{ave} ; (c) variation of back-pressure at max loading, $\Delta p(7\text{ g/L})$ and mass collected per filter channel, m_{ch} ; (d) variation of maximum wall temperature during regeneration, $T_{\text{wall,max}}$. Regeneration triggered by reference filter soot loading ($m_{\text{filt}} = 7\text{ g/L}$).

range [1300–1450 K] and appears to be well correlated to m_{ch} (right axis).

Fig. 7 shows the time history of filter wall temperature, T_{wall} (left column), and soot cake thickness, δ_{cake} (right column), calculated for CPSI 80, 240 and 360 to compare the progress of the soot regeneration process for these three different geometries when regeneration is driven by filter soot loading. Results obtained for CPSI 80 (left column) show that filter wall heats up quickly during regeneration. Burning of soot at each position along the filter completes in about ten seconds, progressing at constant velocity from the upstream to the downstream section of the filter. Compared to Fig. 5, the soot thickness at loading condition is larger, more time is needed for regeneration and a larger amount of heat is produced by soot oxidation. As a consequence, the filter is exposed to larger temperatures for longer times. This is apparent from the evolution of $T_{\text{wall,max}}$ (fourth row) which shows a maximum after 20 s, the time at which regeneration is completed (see right column).

Soot thickness in CPSI 240 is smaller than in CPSI 80 when the regeneration starts, and a bit less homogeneously distributed along the filter length (see right column). The wall temperature profile shows steeper gradients near the channel inlet which become steeper as time goes on moving toward the end of the channel. Propagation of the peak-temperature front and cake oxidation are slower in this case. The largest values of temperature are still found at the end of the channel soon after the regeneration is complete.

The time history of T_{wall} and δ_{cake} calculated for CPSI 360 is

similar to CPSI 240. δ_{cake} is lower at the beginning of regeneration and less homogeneously distributed along the channel; the peak temperature profile and the regeneration efficiency are almost the same as CPSI 240. Comparing the evolution of peak temperature obtained for the different cell densities, we observe that the risk of thermal failure during the first 5 s of regeneration is largest for CPSI 240 and 280, but increases for CPSI 80 later on (from 5 to 20 s after regeneration start) when $T_{\text{wall,max}}$ becomes larger than any other cell density.

The evolution of η_{reg} shows that regeneration is faster for CPSI 80. For this geometry, half of the soot load is burnt after 9.8 s, whereas the regeneration process takes 21 s to complete. For CPSI 240 (and 360), half of the soot load is burnt after 11.6 s (12 s), whereas the regeneration process takes 24.4 s (25 s) to complete.

3.2.2. Effect of clean filter permeability

The use of ceramic materials characterized by controlled pore size and shape and large permeability has proven to be effective for the design of low pressure drop DPFs (see Merkel et al., 2003; Bollerhoff et al., 2012 among others). The permeability controls the pressure drop of the clean filter but affects also the back-pressure build-up during the loading stage. This section presents the results obtained from the simulation of filters made of a larger permeability material (Cordierite or SiC, $k_{w,0} = 28 \cdot 10^{-13}\text{ m}^2$ versus $3.3 \cdot 10^{-13}\text{ m}^2$ of EX-54).

Fig. 8 shows filter performances when the regeneration is triggered by the limiting value of mass loading. Back-pressure build-up versus collected mass per unit volume of filter up to

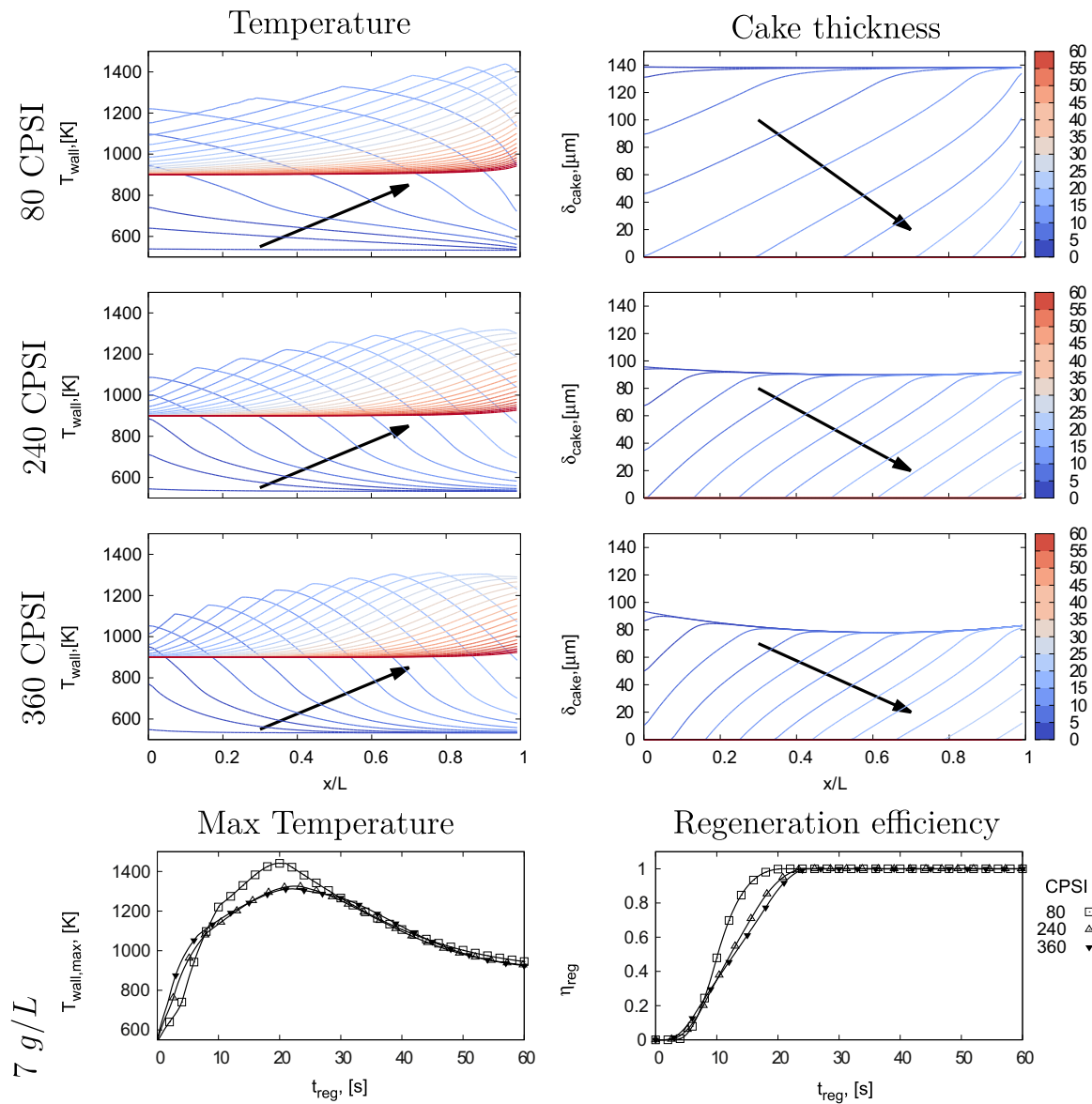


Fig. 7. Time history of filter wall temperature (left) and cake thickness (right) profiles during regeneration for CPSI 80, 240 and 360 filters (rows one to three). Time step is identified by line color (see right legend). Evolution of wall peak temperature, $T_{wall,max}$ (left) and regeneration efficiency, η_{reg} (right) during regeneration (fourth row). Regeneration triggered by reference filter soot loading ($m_{filt} = 7 \text{ g/L}$).

$m_{filt} = 7 \text{ g/L}$ is shown in Fig. 8(a); different symbols identify different CPSI values. For large permeability filters, the steep pressure build-up generally found during deep bed filtration is not observed anymore. Δp_{clean} increases with cell density whereas the rate of back-pressure build-up decreases, being most similar for CPSI values in the range [160–200].

Fig. 8(b) shows more clearly the effect of cell density on Δp_{ave} (right axis). Δp_{clean} is also shown for reference on the same graph (left axis). In this case, Δp_{ave} has a minimum for $CPSI \approx 160\text{--}200$. The trend is similar to that shown in Fig. 4(b), but indicates a different range of cell densities as the optimum for the filter.

Fig. 8(c) shows the values of back-pressure when the filter soot loading is 7 g/L ($\Delta p(7 \text{ g/L})$) (left axis) and the mass collected along each filter channel, m_{ch} (right axis). $\Delta p(7 \text{ g/L})$ has a minimum in the range $CPSI \approx 200\text{--}240$. The mass collected in each channel decreases with increasing cell density.

Fig. 8(d) shows the variation of peak temperature at filter wall (left axis) as a function of cell density. In this case, peak temperature values are bounded within the range [1305–1365 K]. Different from the low permeability case (see Fig. 6(d)) the

maximum temperature reached by the filtering medium during regeneration appears to be not well correlated as before to m_{ch} (right axis) for $CPSI < 200$.

Fig. 9 shows the time history of filter wall temperature (left column) and soot cake thickness (right column) calculated for CPSI 80, 240 and 360 (rows 1–3) in the case of the large permeability support. Results obtained for CPSI 80 indicate that filter wall heats up and soot oxidation proceeds faster in the first part of the channel, slowing down in the downstream portion. The soot oxidation rate decreases over time as the regeneration front moves at downstream positions along the filter. Compared to Fig. 7, the evolution of peak temperature (last row) is characterized by a flatter profile during the regeneration.

The soot thickness in CPSI 240 is smaller than in CPSI 80 when the regeneration starts, and a bit less homogeneously distributed along the filter length (see right column). The propagation of the thermal wave and the reduction of cake thickness is faster in the upstream portion of the channel, slows down in the central part and increases slightly again at the end of the channel. The largest values of temperature are still found at the end of the channel

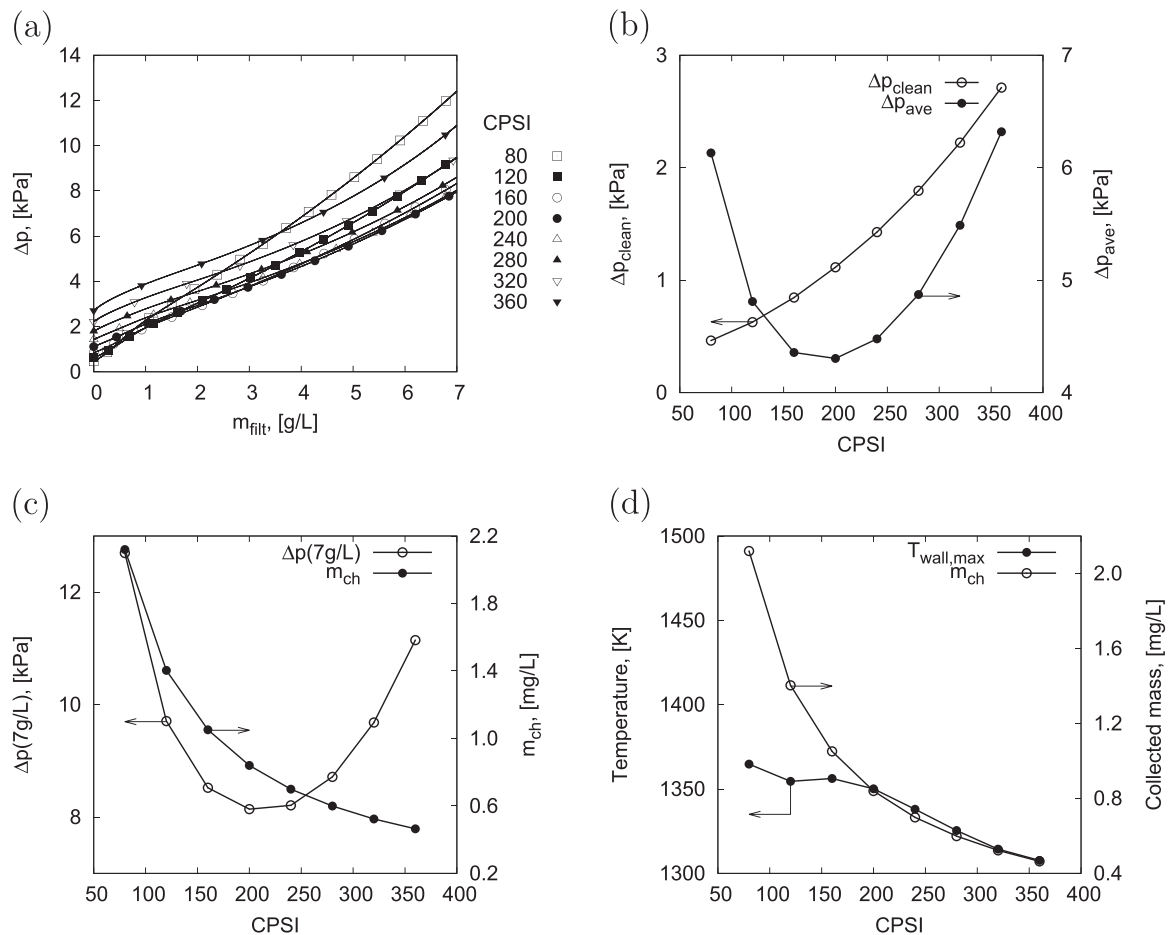


Fig. 8. Effect of cell density in large permeability filter: (a) back-pressure, Δp , build-up over time during the loading stage; (b) variation of clean filter, Δp_{clean} , and time averaged back-pressure, Δp_{ave} ; (c) variation of back-pressure at max loading, $\Delta p(7\text{g/L})$ and mass collected per filter channel, m_{ch} ; (d) variation of maximum wall temperature during regeneration, $T_{\text{wall,max}}$. Regeneration triggered by reference filter soot loading ($m_{\text{filt}} = 7\text{g/L}$).

soon after the end of the regeneration.

The time history of temperature and soot cake thickness profiles calculated for CPSI 360 is similar to CPSI 240. Nevertheless, at the beginning of the regeneration the soot thickness along the channel is lower and much more unevenly distributed. Soot oxidation completes in about 6 s at the upstream end of the filter, needs more than 12 s to complete half distance along the channel and again needs less than 8 s to complete at the downstream end.

The variation in time of η_{reg} shows that regeneration for CPSI 80 is faster than for larger cell densities at the beginning and slows down at later times. For this cell density, half of the soot load is burnt after 10.2 s, whereas the regeneration process takes 35.4 s to complete. For CPSI 240 (and 360), half of the soot load is burnt after 13 s (13.6 s), whereas the regeneration process takes 27.2 s (25.8 s) to complete.

3.2.3. Effect of heat capacity

Ceramic substrates characterized by small or large heat capacity can be used to control the rate of temperature rise and the peak temperature value inside the DPF. Optimal thermal management of DPFs is obtained when filter characteristics and regeneration conditions allow for fast, reliable and safe burning of accumulated soot (Boger et al., 2008). Tanner et al. (2015) studied and tested the use of substrates with reduced heat capacity to accelerate the filter thermal response under cold starts. On the other hand, the increase of DPF thermal inertia by materials of large specific heat capacity limits the rate at which heat can be stored and released by the filter, damping also the temperature

variation. In this section, we evaluate the performances of filter substrates characterized by large specific heat capacity (e.g. Aluminum Titanate, AT, $c_{p,\text{wall}} = 2000\text{ J/kg K}$ versus 1300 J/kg K of EX-54).

No variation of back-pressure build-up is expected during the loading stage by changing the specific heat capacity of the filter support. Variations are expected for the peak wall temperature, since the thermal inertia determines the rate of temperature change of the filter and, as a direct consequence, the rate of heat release due to the thermal oxidation of soot. Fig. 10 shows the variation of peak temperature at filter wall, $T_{\text{wall,max}}$ (left axis), associated to a large specific heat capacity filter (open triangles). Even if the soot mass loading per channel, m_{ch} , is unchanged (right axis), $T_{\text{wall,max}}$ turns to be about 200 K lower than for the standard heat capacity filter (solid circles).

Fig. 11 shows the time history of filter wall temperature (left column) and soot cake thickness (right column) calculated for CPSI 80, 240 and 360 in the case of filter support characterized by large permeability and large specific heat capacity. Results obtained for CPSI 80 indicate that the larger thermal inertia slows down the propagation of the thermal wave along the filter channel. Wall temperature increases more gradually and the soot oxidation rate reduces, determining a more gradual propagation of the regeneration front. Compared to Fig. 9, more time is needed for regeneration and the heat produced by soot combustion is more homogeneously distributed along the filter and over time, with a decrease of peak temperature value.

Also for CPSI 240 the propagation of the peak-temperature

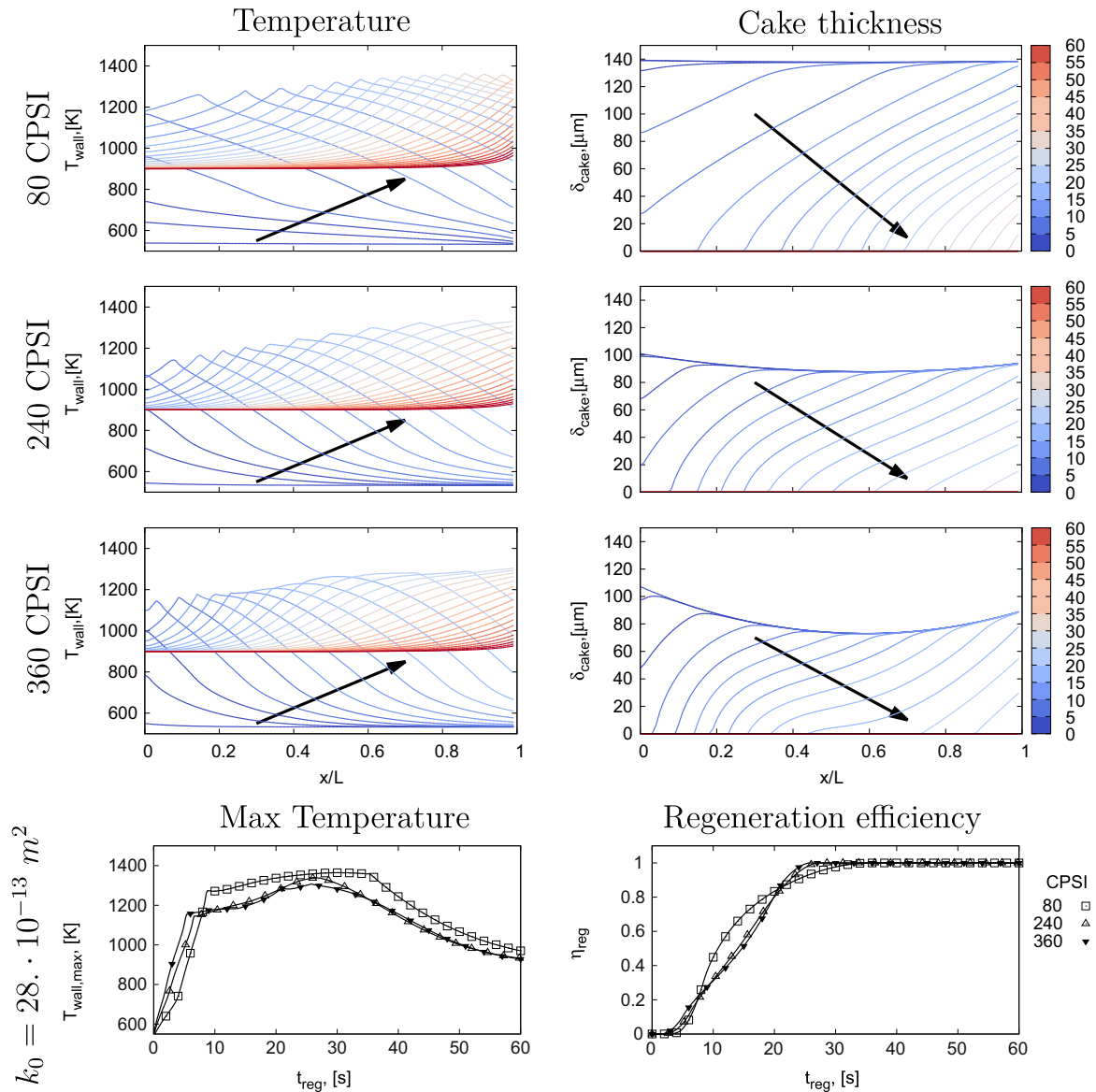


Fig. 9. Time history of filter wall temperature (left) and cake thickness (right) profiles during regeneration for CPSI 80, 240 and 360 filters (rows one to three). Time step is identified by line color (see right legend). Support characterized by high hydraulic permeability. Evolution of wall peak temperature, $T_{wall,max}$ (left), and regeneration efficiency, η_{reg} (right), during regeneration (fourth row). Regeneration triggered by reference filter soot loading ($m_{filt} = 7 \text{ g/L}$).

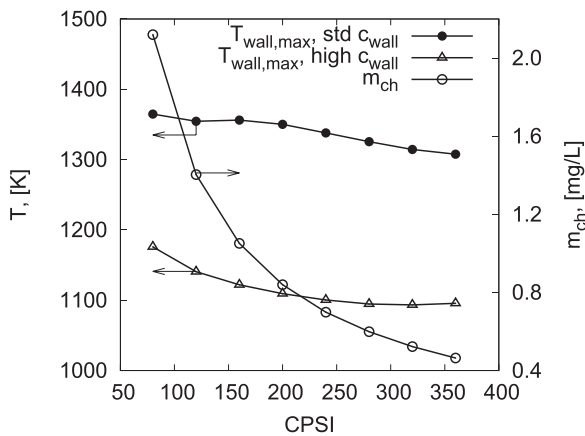


Fig. 10. Effect of heat capacity: comparison between max peak temperature values (left axis) calculated for $c_{wall} = 1300 \text{ J/kg K}$ (closed circles) and $c_{wall} = 2000 \text{ J/kg K}$ (open triangles) as a function of CPSI. Mass collected per filter channel is shown on the right axis.

front and the reduction of cake thickness become slower and more regular in time. The same value of peak temperature but this value is significantly reduced compared to the standard heat capacity support.

The time history of temperature and soot cake thickness calculated for CPSI 360 is similar to CPSI 240. Compared with Fig. 9, the propagation of the thermal front and of the regeneration front are delayed but develop neatly in time.

The evolution of η_{reg} shows that regeneration is delayed for all CPSI values. For CPSI 80, half of the soot load is burnt after 19.2 s, whereas the regeneration process takes 46 s to complete. For CPSI 240 (and 360), half of the soot load is burnt after 24.2 s (25 s), whereas the regeneration process takes 44 s (43.8 s) to complete.

4. Conclusion

In this work a semi-analytical, one dimensional model was developed to predict variations of filter performances during both loading and regeneration stage when filter channels of different

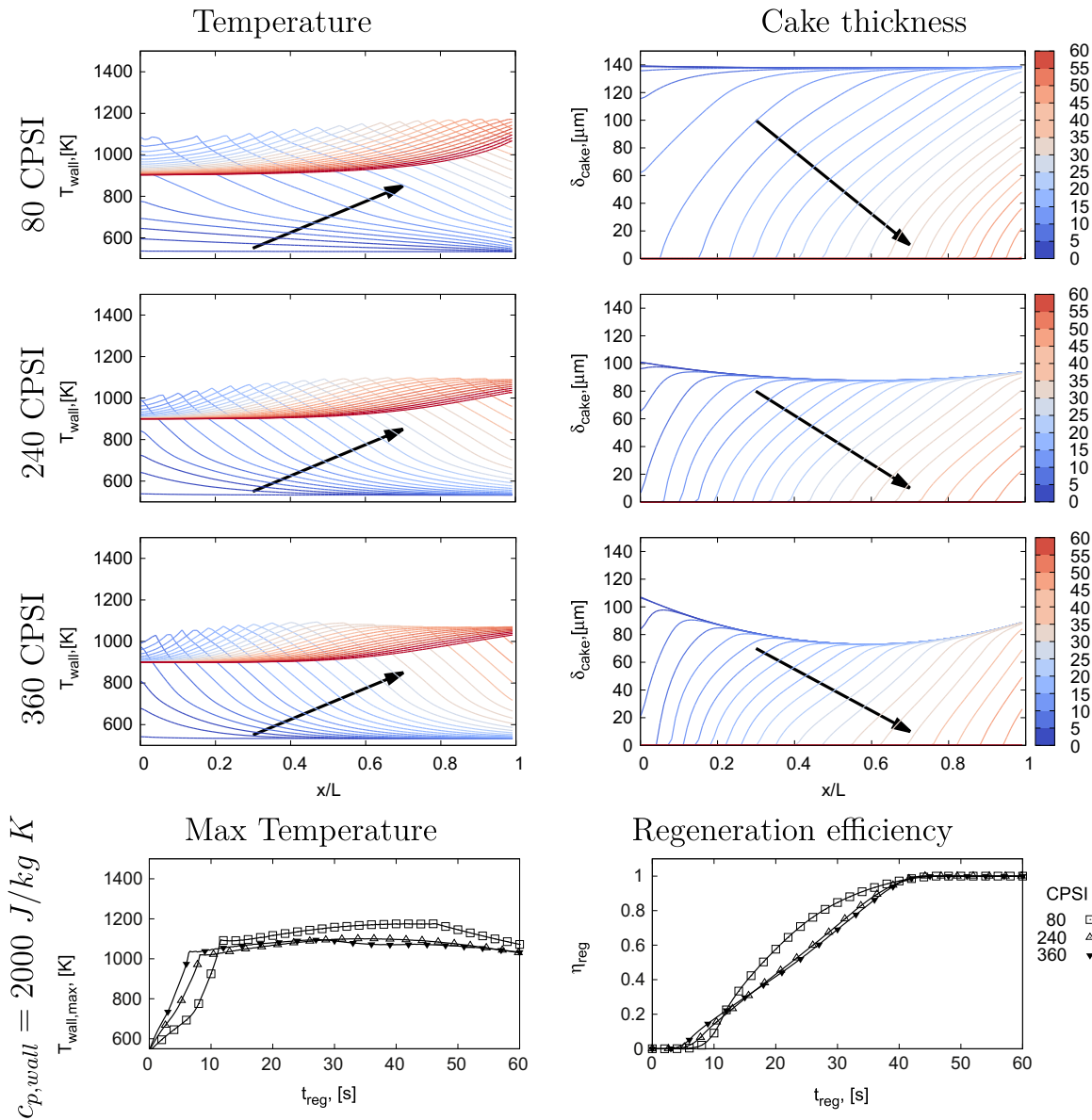


Fig. 11. Time history of filter wall temperature (left) and cake thickness profiles during regeneration for CPSI 80, 240 and 360 filters (rows one to three). Time step is identified by line color (see right legend). Support characterized by large hydraulic permeability and large heat capacity. Evolution of wall peak temperature, $T_{wall,max}$ (left) and regeneration efficiency, η_{reg} (right) during regeneration (fourth row). Regeneration triggered by reference filter soot loading ($m_{fit} = 7 \text{ g/L}$).

size and ceramic material are used. The model has been validated with experimental data available from the literature and used to evaluate the impact of cell density, filter hydraulic permeability and thermal specific capacity on filter back-pressure build up, regeneration efficiency and risk of thermal failure of the filter.

The comparative evaluation of the build-up of back-pressure profiles during loading operations indicates that, for standard permeability filters, cell densities in the range [240–280] represent the optimal choice (i) maximizing filter loading capacity (when regeneration is triggered by back-pressure exceeding a reference threshold) or (ii) minimizing the value of back-pressure averaged over the loading cycle (when regeneration is triggered by a reference soot loading value). Values of optimal cell densities change if different filter materials are used. For filtering support characterized by larger permeability, the optimal range of cell densities moves toward lower CPSI values [160–200].

The comparative evaluation of filter behavior during

regeneration indicates that improved thermal management of the filter can be obtained by tuning cell density simultaneously with properties of filter support. Larger hydraulic permeability in standard heat capacity filter delays soot oxidation extending the high temperature exposure of filter support. Larger hydraulic permeability in large heat capacity filter regularize soot oxidation inside the filter reducing the high temperature exposure of filter support.

Acknowledgements

Financial support from Regione Autonoma Friuli Venezia Giulia under the research project “Sviluppo di filtri catalitici e anti-particolato ad alta efficienza per una sostenibile mobilità compatibile con Euro 6” is gratefully acknowledged.

Appendix A

A.1. Deep bed and cake filtration sub-models

A.1.1. Partition coefficient

The fraction of soot mass moving into the filter is given by $d\dot{m}_{bed} = \Phi d\dot{m}_{sep}$ where the partition coefficient Φ is defined as

$$\Phi = \frac{d_c(t)^3 - d_c(0)^3}{(\psi b^3) - d_c(0)^3} \in [0, 1] \quad (21)$$

It depends on the mass already collected (upper term, representing the increasing value of the unit collector diameter, $d_c(t)$, from starting time, $d_c(0)$) and the maximum mass which can be stored in the wall layer (lower term, with b and $\psi \in [0, 1]$ representing the maximum value for $d_c(t)$ and the percolation factor, respectively). Values of Φ decreasing over time indicate the increasing importance of cake filtration compared to deep bed filtration.

A.1.2. Deep bed filtration efficiency

The filter porous wall is modelled as a multilayer bed of packed spheres. The initial porosity of the layer (ϵ_0) and the mean pore size ($d_{p,0}$) are used to define the size of the reference unit collector $d_{c,0}$ and its packing b :

$$d_{c,0} = \frac{3(1 - \epsilon_0)}{2\epsilon_0} d_{p,0} b = \frac{d_{c,0}}{(1 - \epsilon_0)^{1/3}} \quad (22)$$

which are used for the calculation of collection efficiency, E_i . Collection efficiency, η , is calculated from the joint effect of diffusion, interception and impaction mechanisms (see Lee and Gieseke, 1979)

$$E_i = 1 - \exp\left[-\frac{3(1 - \epsilon)\eta\delta_i}{2\epsilon d_c}\right] \quad (23)$$

which depends on the local porosity (ϵ), size of collectors (d_c) and layer thickness (δ_i); the mass collected in each layer per unit collector $\dot{m}_{col,uc}$ modifies the unit collector size

$$d_c(t) = \left(d_{c,0}^3 + \frac{6}{\pi} \frac{\dot{m}_{col,uc}}{\rho_{soot,wall}}\right)^{1/3} \quad (24)$$

and the local properties of wall layer such as the porosity

$$\epsilon(t) = 1 - \left(1 - \epsilon_0\right) \left[\frac{d_c(t)}{d_{c,0}}\right]^3 \quad (25)$$

and the permeability

$$k_w(t) = k_{w,0} \frac{f(\epsilon) d_c^2}{f(\epsilon_0) d_{c,0}^2} \quad (26)$$

Any of the expressions reported by Konstandopoulos (2003) can be used for $f(\epsilon)$ since they are equivalent in the range of porosity of interest. Overall soot collection inside the wall layer is obtained as the multistage filtration efficiency of the number of simulated layers, n_i :

$$E_{tot} = 1 - \prod_{i=1}^{n_i} (1 - E_i) \quad (27)$$

References

Adler, J., 2005. Ceramic diesel particulate filters. *Int. J. Appl. Ceram. Technol.* 2 (6), 429–439.

Bahrami, M., Yovanovich, M.M., Culham, J.R., 2006. Pressure drop of fully-developed laminar flow in microchannels of arbitrary cross-section. *J. Fluids Eng.* 128 (5), 1036–1044.

Bensaid, S., Marchisio, D.L., Russo, N., Fino, D., 2009a. Experimental investigation of

soot deposition in diesel particulate filters. *Catal. Today* 147, S295–S300.

Bensaid, S., Marchisio, D.-L., Fino, D., Saracco, G., Specchia, V., 2009b. Modelling of diesel particulate filtration in wall-flow traps. *Chem. Eng. J.* 154 (1), 211–218.

Bensaid, S., Marchisio, D.L., Fino, D., 2010. Numerical simulation of soot filtration and combustion within diesel particulate filters. *Chem. Eng. Sci.* 65 (1), 357–363.

Bensaid, S., Caroca, C.J., Russo, N., Fino, D., 2011. Detailed investigation of non-catalytic DPF regeneration. *Can. J. Chem. Eng.* 89 (2), 401–407.

Bissett, E.J., 1984. Mathematical model of the thermal regeneration of a wall-flow monolith Diesel Particulate Filter. *Chem. Eng. Sci.* 39, 1233–1244.

Bissett, E.J., 1985. Thermal regeneration of particle filters with large conduction. *Math. Model.* 6 (1), 1–18.

Bissett, E.J., Kostoglou, M., Konstandopoulos, A.G., 2012. Frictional and heat transfer characteristics of flow in square porous tubes of wall-flow monoliths. *Chem. Eng. Sci.* 84, 255–265.

Boger, T., Rose, D., Tilgner, Ingo-C., Heibel, A.K., 2008. Regeneration Strategies for an Enhanced Thermal Management of Oxide Diesel Particulate Filters. SAE Paper 01-0328.

Bollerhoff, T., Markomanolakis, I., Koltsakis, G., 2012. Filtration and regeneration modeling for particulate filters with inhomogeneous wall structure. *Catal. Today* 188, 24–31.

Chen, K., Sun, T., 2013. Nonuniformity behavior during regeneration of the diesel particulate filter. *Asia-Pac. J. Chem. Eng.* 8 (6), 922–930.

Deuschle, T., Janoske, U., Piesche, M., 2008. A CFD-model describing filtration, regeneration and deposit rearrangement effects in gas filter systems. *Chem. Eng. J.* 135 (1–2), 49–55.

Konstandopoulos, A.G., Kostoglou, M., Skaperdas, E., Papaioannou, E., Zarvalis, D., Kladopoulou, E., 2000. Fundamental Studies of Diesel Particulate Filters: Transient Loading, Regeneration and Aging. SAE Paper 01-1016.

Konstandopoulos, A.G., 2003. Flow Resistance Descriptors for Diesel Particulate Filters: Definitions, Measurements and Testing. SAE Paper 01-0846.

Kostoglou, M., Bissett, E.J., Konstandopoulos, A.G., 2012. Improved transfer coefficients for wall-flow monolithic catalytic reactors: energy and momentum transport. *Ind. Eng. Chem. Res.* 51 (40), 13062–13072.

Lee, K.W., Gieseke, J.A., 1979. Collection of aerosol particles by packed beds. *Env. Sci. Technol.* 13 (4), 466–470.

Lee, S.J., Jeong, S.J., Kim, W.S., 2009. Numerical design of the diesel particulate filter for optimum thermal performances during regeneration. *Appl. Energy* 86 (7–8), 1124–1135.

Liati, A., Eggenschwiler, P.D., 2010. Characterization of particulate matter deposited in diesel particulate filters: visual and analytical approach in macro-, micro- and nano-scales. *Combust. Flame* 157 (9), 1658–1670.

Liati, A., Spiteri, A., Eggenschwiler, P.D., Vogel-Schauble, N., 2012. Microscopic investigation of soot and ash particulate matter derived from biofuel and diesel: implications for the reactivity of soot. *J. Nanopart. Res.* 14 (11), 1224.

Martirosyan, K.S., Chen, K., Luss, D., 2010. Behavior features of soot combustion in diesel particulate filter. *Chem. Eng. Sci.* 65 (1), 42–46.

Merkel, G.A., Cutler, W.A., Tao, T., Chiffey, A., Phillips, P., Twigg, M.V., Walker, A., 2003. New Cordierite diesel particulate filters for catalyzed and non-catalyzed applications. In: Proceedings of the 9th Diesel Emission Reduction Conference, August 24–28, 2003, Newport, Rhode Island.

Murtagh, M.J., Sherwood, D.L., Socha, L.S., 1994. Development of a Diesel Particulate Filter Composition and Its Effect on Thermal Durability and Filtration Performance. SAE Paper, 2014, 04-30.

Nemoto, A., Iwasaki, K., Yamanishi, O., Tsuchimoto, K., Uoe, K., Toma, T., Yoshino, H., 2011. Development of Innovative Diesel Particulate Filters Based on Aluminum Titanate: Design and Validation. Sumitomo Kagaku, 2011-II.

Nova, I., Bounechada, D., Maestri, R., Tronconi, E., Heibel, A.K., Collins, T.A., Boger, T., 2011. Influence of the substrate properties on the performances of NH₃-SCR monolithic catalysts for the aftertreatment of diesel exhaust: an experimental and modeling study. *Ind. Eng. Chem. Res.* 50 (1), 299–309.

Park, K., Kittelson, D.B., McMurry, P.H., 2004. Structural properties of diesel exhaust particles measured by transmission electron microscopy (TEM): relationships to particle mass and mobility. *Aerosol Sci. Technol.* 38 (9), 881–889.

Sakashita, S., Hirakawa, T., 2013. Filter Element. Patent US2013/0239532, September 19, 2013.

Piscaglia, F., Ferrari, G., 2009. A novel 1D approach for the simulation of unsteady reacting flows in diesel exhaust after-treatment systems. *Energy* 34 (12), 2051–2062.

Saad, Y., Wu, K.S., 1995. Design of an iterative solution module for a parallel sparse matrix library (P-SPARSLIB). *Appl. Numer. Math.* 19 (3), 343–357.

Sbrizzai, F., Faraldi, P., Soldati, A., 2005. Appraisal of three-dimensional numerical simulation for sub-micron particle deposition in a micro-porous ceramic filter. *Chem. Eng. Sci.* 60 (23), 6551–6563.

Schejbal, M., Marek, M., Kubiček, M., Kočí, P., 2009. Modelling of diesel filters for particulates removal. *Chem. Eng. J.* 154 (1), 219–230.

Serrano, J.R., Arnau, F.J., Piqueras, P., García-Afonso, O., 2013. Packed bed of spherical particles approach for pressure drop prediction in wall-flow DPFs (diesel particulate filters) under soot loading conditions. *Energy* 58, 644–654.

Soldati, A., Campolo, M., Sbrizzai, F., 2010. Modeling nano-particle deposition in diesel engine filters. *Chem. Eng. Sci.* 65 (24), 6443–6451.

Soldati, A., Marchioli, C., 2009. Physics and modelling of turbulent particle deposition and entrainment: review of a systematic study. *Int. J. Multiph. Flow* 35, 827–839.

Stanmore, B.R., Brilhac, J.F., Gilot, P., 2001. The oxidation of soot: a review of experiments, mechanisms and models. *Carbon* 39 (15), 2247–2268.

- Strom, H., Sasic, S., Andersson, B., 2011. Effects of the turbulent-to-laminar transition in monolithic reactors for automotive pollution control. *Ind. Eng. Chem. Res.* 50, 3194–3205.
- Tandon, P., Heibel, A., Whitmore, J., Kekre, N., Chithapragada, K., 2010. Measurement and prediction of filtration efficiency evolution of soot loaded diesel particulate filters. *Chem. Eng. Sci.* 65 (16), 4751–4760.
- Tanner, C.W., Twiggs, K., Tao, T., Bronfenbrenner, D., Matsuzono, Y., Otsuka, S., Suehiro, Y., Koyama, H., 2015. High porosity substrates for fast light-off applications. *SAE Paper* 01-1009.
- Tsuneyoshi, K., Yamamoto, K., 2012. A study on the cell structure and the performances of wall-flow diesel particulate filter. *Energy* 48 (1), 492–499.